POLITECNICO DI TORINO
Repository ISTITUZIONALE

Does the inflow velocity profile influence physiologically relevant flow patterns in computational hemodynamic models of left anterior descending coronary artery?

(Article begins on next page)

16 July 2022

Does the inflow velocity profile influence physiologically relevant flow patterns in computational hemodynamic models of left anterior descending coronary artery?

Maurizio Lodi Rizzini[1], Diego Gallo[1], Giuseppe De Nisco[1], Fabrizio D'Ascenzo[2], Claudio Chiastra[1], Pier Paolo Bocchino[2], Francesco Piroli[2], Gaetano Maria De Ferrari[2], Umberto Morbiducci[1]

1. PoliTo[BIO]Med Lab, Department of Mechanical and Aerospace Engineering, Politecnico di Torino, Torino, Italy
2. Hemodynamic Laboratory, Department of Medical Sciences, University of Turin, Turin, Italy

Address for correspondence:

Prof. Umberto Morbiducci

PoliTo[BIO]Med Lab, Department of Mechanical and Aerospace Engineering

Politecnico di Torino

Corso Duca degli Abruzzi 24

10129 Turin, Italy

Tel.: +39 011 0906882

E-mail: umberto.morbiducci@polito.it

Abstract

Patient-specific computational fluid dynamics is a powerful tool for investigating the hemodynamic risk in coronary arteries. Proper setting of flow boundary conditions in computational hemodynamic models of coronary arteries is one of the sources of uncertainty weakening the findings of *in silico* experiments, in consequence of the challenging task of obtaining *in vivo* 3D flow measurements within the clinical framework. Accordingly, in this study we evaluated the influence of assumptions on inflow velocity profile shape on coronary artery hemodynamics. To do that, (1) ten left anterior descending coronary artery (LAD) geometries were reconstructed from clinical angiography, and (2) eleven velocity profiles with realistic 3D features such as eccentricity and differently shaped (single- and double-vortex) secondary flows were generated analytically and imposed as inflow boundary conditions. Wall shear stress and helicity-based descriptors obtained prescribing the commonly used parabolic velocity profile were compared with those obtained with the other velocity profiles. Our findings indicated that the imposition of idealized velocity profiles as inflow boundary condition is acceptable as long the results of the proximal vessel segment are not considered, in LAD coronary arteries. As a pragmatic rule of thumb, a conservative estimation of the length of influence of the shape of the inflow velocity profile on LAD local hemodynamics can be given by the theoretical entrance length for cylindrical conduits in laminar flow conditions.

Keywords

1. Introduction

The marked predisposition to develop atherosclerosis makes coronary arteries of paramount clinical relevance. Although atherosclerosis initiation and progression results from the interplay of many systemic factors [1], its development at specific, geometrically predisposed locations such as branching and bifurcations [2] suggested the involvement of local hemodynamics [3,4]. In particular, the role of wall shear stress (WSS) was extensively investigated over the last years [5–8], while more recently the role of intravascular helical patterns on coronary atherosclerosis initiation and progression was demonstrated [9,10]. In this context, the combined use of medical imaging and computational fluid dynamics (CFD) has proven to be a valuable tool in the study of possible associations between local hemodynamics and coronary artery disease as it makes available highly resolved hemodynamic flow patterns inside anatomically realistic, patient-specific geometries [11–13]. However, *in silico* methods require assumptions that introduce uncertainties, weakening CFD findings at a level that could limit their translation to clinics [14–20]. As recently highlighted, the uncertainties in cardiovascular modelling should not compromise its added value with respect to standard clinical measurement and therefore they should be carefully assessed.

While anatomically realistic geometries can be reconstructed with satisfactory accuracy using *in vivo* imaging tools, acquiring non-defective patient-specific boundary conditions, as required to perform reliable computational hemodynamics, is not always feasible. This is particularly true for the coronary arteries, for which (1) the measurable (whenever possible) inflow rates can be imposed only in terms of idealized velocity profiles, and (2) the possibility to use realistic three-dimensional (3D) velocity profiles measured directly *in vivo* as inflow boundary condition is still challenging, due to issues related to resolution and cardiac motion

[21]. To be clearer, when only the integral quantity flow rate is available, its translation to inflow Dirichlet boundary condition in terms of 3D velocity profiles in CFD applications necessarily undergoes an idealization process based on a priori hypotheses to fill the gap of information. For these reasons, most of the previous computational studies on coronary arteries, including those accounting for the presence of coronary stents, starting from *in vivo* flow rate measurements/estimations, prescribed the inflow boundary conditions in terms of flat (e.g. [22–25]) or fully developed (e.g. [26–30]) velocity profiles. Such a priori hypotheses on the velocity profiles to be used as conditions at inflow boundaries represent a source of uncertainty in the estimation of helical and WSS patterns [31], potentially masking their relationship with atherosclerosis initiation and progression. Moreover, *in vitro* and *in silico* hemodynamic studies revealed the presence of skewed velocity profiles in the left coronary artery [32–34], with a not negligible presence of secondary flows in the entire coronary tree, as it can be expected by considering the vessel tortuosity and the presence of bifurcations and branching.

In this context, the aim of this study was to evaluate the budget of uncertainty associated with assumptions on the shape of the velocity profiles imposed as inflow boundary conditions in coronary artery CFD models. To this end, a framework was developed enabling the generation of artificial velocity profiles by means of generalized analytical formulations able to (1) generate 3D velocity profiles with secondary flows, and (2) fit the non-circular cross-section of blood vessels. The developed framework was then applied to left anterior descending (LAD) coronary artery models to evaluate the impact that the shape of inflow velocity profiles used as inlet boundary condition has on WSS distribution at the luminal surface and intravascular flow features, focusing on helical flow patterns.

2. Materials and methods

2.1 Image data collection and 3D vessel reconstruction

Ten subjects (8 males and 2 females, age = 58.6±6.5) that underwent invasive coronary cineangiography after heart transplant with no sign of atherosclerosis were selected for this study. Clinical images were acquired at Città della Salute e della Scienza hospital (Turin, Italy) with the monoplane X-ray system Allura Xper (Philips Medical Systems, Amsterdam, The Netherlands). Two cranial, end-diastolic angiographic projections, with a minimum angle of 25° between them were used to reconstruct the geometry of the LAD coronary arteries using the commercial software QAngio XA Bifurcation RE (Medis medical imaging systems, Leiden, The Netherlands). The study complies with the Declaration of Helsinki on human research and was approved by the Città della Salute e della Scienza hospital. All patients gave written informed consent.

Given the importance of side branches for hemodynamic characterization of coronary arteries [22,35–37], each side branch with a diameter greater than 1 millimetre was reconstructed and merged to form the LAD geometry using VTK (Kitware, Inc., Clifton Park, NY, USA) and VMTK (Orobix, Bergamo, Italy) libraries. Technically, the main vessel was segmented and reconstructed considering one side branch at a time, repeating this operation for all side branches (Figure 1A). Then, the Voronoi diagrams computed over each bifurcation were combined into a single diagram to obtain the complete 3D geometry including all side branches. The final result of the 3D LAD geometry reconstruction process is presented in Figure 1B. All LAD geometries present two diagonals branches and one septal branch.

2.2 Computational hemodynamics and boundary conditions

The governing equations of fluid motion were solved in their discretized form under steady-state conditions using the finite volume method with the general purpose CFD software Fluent (Ansys Inc., Canonsburg, PA). The fluid domain was discretized by means of the meshing software ICEM CFD (Ansys Inc., Canonsburg, PA, USA) using tetrahedral elements with curvature-based refinement and 5 near-wall prismatic layers. The same meshing parameters derived from a previous grid independence analysis were adopted [9,10], resulting in a mesh cardinality ranging between 1.7 and 5.5 million elements, depending on vessel total volume and local curvature. The blood was assumed as a homogeneous, incompressible fluid with a density ρ equal to 1060 Kg/m^3. The blood non-Newtonian behaviour was modelled using the Carreau model (μ_∞ = 0.0035 Pa·s, μ_0 = 0.25 Pa·s, λ = 25 s, and n=0.25) [38]. The vessel walls were assumed to be rigid and no-slip condition was applied at wall boundaries. Details on CFD settings are extensively described elsewhere [38]. Concerning the inlet and outlet boundary conditions, since *in vivo* measured data were not available, inlet flow rates were obtained using a scaling law based on the hydraulic diameter of the inlet cross-section [39]. The resulting inlet flow rates (mean = 43.12 mL/min, range: 30.73 to 70.99 mL/min) were prescribed in terms of 3D velocity profiles at the inlet, as detailed in the following section. As for outlets, the flow split at each bifurcation was estimated using a scaling law based on the ratio of the hydraulic diameter of the daughter branches [39], and imposed as outflow boundary condition.

2.3 3D velocity profiles generation: analytical formulation

The 3D velocity profile on a generic cross-section of a vessel can be described as a combination of (1) a principal, through-plane (TP) component, in the direction of the axis of the vessel, and (2) a secondary, in-plane (IP) component, lying on the plane orthogonal to the axis of

the vessel. To test the impact of the velocity profile on the hemodynamics of LAD coronary arteries, different 3D velocity profiles were generated using analytical formulations based on previous observations demonstrating the presence of secondary flows in coronary arteries [32,34].

To deal with realistic non-circular cross-section of vessels, a generalized polar coordinate system was here introduced. More in detail, starting from the polar coordinate system (r, ϑ) defined on a generic vessel cross-section, a new generalized polar coordinate system (r', ϑ') was defined on the inflow section of each LAD vessel as:

$$\begin{cases} r' = \frac{r}{R(\vartheta)} \\ \vartheta' = \vartheta \end{cases} \tag{1}$$

where R(ϑ) is the variable radius of the inlet surface depending on angular coordinate. By construction, r' can assume values in the range [0, 1]. Once the new coordinate system has been defined, the TP component was obtained using a generalized formulation of parabolic velocity profile:

$$\boldsymbol{v}_{TP}(r', \vartheta') = [1 - r'^2 + Kr'(r'^2 - 1)\cos(\vartheta')]\boldsymbol{u}_n \tag{2}$$

where K is a constant regulating the displacement of peak velocity from the geometric centre of the inlet cross-section, and $\boldsymbol{u}_n$ is the unit vector in the vessel axis direction. Two differently shaped TP velocity profiles were built prescribing K = 0 and K = 1, to obtain a parabolic and a skewed velocity profile (i.e., with the $\boldsymbol{v}_{TP}(r', \vartheta')$ maximum value dislodged from vessel axis), respectively (Figure 2A).

Secondary flows as part of the 3D velocity profile were incorporated considering two possible configurations, namely (1) the single-vortex, and (2) the Dean-like double-vortex

configurations. The first configuration was obtained by generalizing the equation previously

proposed to describe axially symmetric flow rotations [40] as follows:

$$\begin{cases} \boldsymbol{v}_{\vartheta\prime}(\mathrm{r}',\vartheta') = \mathrm{r}'(1-\mathrm{r}'^2)\boldsymbol{u}_{\vartheta\prime} \\ \boldsymbol{v}_{r\prime}(\mathrm{r}',\vartheta') = 0 \cdot \boldsymbol{u}_{r\prime} \end{cases} \tag{3}$$

where $\boldsymbol{u}_{\vartheta\prime}$ and $\boldsymbol{u}_{r\prime}$ are the unit vectors in angular and radial directions, respectively. The second

configuration was obtained generalizing the Dean theory for secondary flows in curved pipes

[41] as follows:

$$\begin{cases} \boldsymbol{v}_{\vartheta\prime}(\mathrm{r}',\vartheta') = (1-\mathrm{r}'^2)(4-23\mathrm{r}'^2+7\mathrm{r}'^4)\cos\vartheta'\,\boldsymbol{u}_{\vartheta\prime} \\ \boldsymbol{v}_{r\prime}(\mathrm{r}',\vartheta') = (1-\mathrm{r}'^2)^2(4-\mathrm{r}'^2)\sin\vartheta'\,\boldsymbol{u}_{r\prime} \end{cases} \tag{4}$$

The IP velocity vector was scaled with respect to the TP component as follows:

$$\boldsymbol{v}_{IP}(\mathrm{r}',\vartheta') = C\,\frac{v_{\vartheta\prime}(\mathrm{r}',\vartheta')+v_{r\prime}(\mathrm{r}',\vartheta')}{|v_{\vartheta\prime}(\mathrm{r}',\vartheta')+v_{r\prime}(\mathrm{r}',\vartheta')|}\,\overline{(\boldsymbol{v}_{TP}\cdot\boldsymbol{u}_n)} \tag{5}$$

where C is a scaling factor. In this study, we imposed C=±0.25, corresponding to an IP velocity

component equal to the 25% of TP velocity component. The sign of constant C was used to

generate secondary flows that differ in the direction of rotation, while a scaling factor C=0 was

used to generate purely TP velocity profiles.

Ten different inflow velocity profiles were generated combining all the TP and IP

configurations mentioned above and imposed as inflow boundary conditions to the ten LAD

models. The analysis was completed by prescribing a flat velocity profile, corresponding to plug

flow and representing the simplest boundary condition to be imposed, resulting in a total

number of 110 simulations.

In the followings, the generated velocity profiles are identified according to a code

composed by the applied value of constant K, the number of vortices characterizing the

secondary flows, and the value of constant C (e.g., 0_1V_0.25 for a parabolic velocity profile, with

single-vortex IP component rotating in counter-clockwise direction). The differently shaped generated velocity profiles are displayed in Figure 2C.

2.4 Hemodynamic descriptors

The impact of the shape of inflow velocity profiles on LAD blood flow was evaluated in terms of near-wall and intravascular hemodynamic descriptors. In general, the quantitative comparison was carried out assuming as reference case the purely TP parabolic (0_0V_0.00) velocity profile [26,28,29].

Near-wall hemodynamics was investigated in terms of wall shear stress magnitude (|**WSS**|) distribution over the luminal surface. In addition, for each simulation the surface averaged |**WSS**| value (AWSS) was computed as follows:

$$\text{AWSS} = \frac{1}{S} \int_S |\boldsymbol{WSS}(\boldsymbol{x})| \mathrm{dS}$$ (6)

where $\boldsymbol{x}$ is the position vector and S is the generic luminal surface. Here, four regions were considered as integration surface: the whole main vessel, the LAD proximal, mid and distal segments (Figure 1A), delimited by diagonal branches and defined in accordance with the American Heart Association classification [42]. To quantify the distance downstream of the inflow section of the LAD model where the shape of the inflow velocity profile still influences near-wall hemodynamics, the cross-section averages of the local |**WSS**| values were analysed moving along the centreline of the vessel. Then, impact length of the inflow velocity profile shape was defined as the distance from the LAD inflow section at which differences in cross-sectional average |**WSS**| values falls below 5%, when compared to the cross-sectional average |**WSS**| values obtained imposing the reference velocity profile. Such distance was expressed in terms of cross-sectional hydraulic diameter of the LAD inflow section. The velocity profile shape length of

influence was then compared with the theoretical "entrance length", calculated for each LAD model according to the formulation valid for fully developed laminar flows in cylindrical pipes [43]:

$$L = 0.05 \cdot \text{Re} \tag{7}$$

where L is expressed in terms of number of hydraulic diameters of the inflow section, and Re is the Reynolds number characterizing the flow field in the LAD model.

The impact of the shape of the inflow velocity profile on physiologically relevant intravascular flow features was also investigated. Motivated from very recent findings demonstrating the atheroprotective role of helical flow in coronary arteries [9,10], here the fluid mechanic quantity helicity was considered and helicity-based descriptors proposed elsewhere were analysed [44–46]. In particular, helical flow was visualized in terms of local normalized helicity (LNH) isosurfaces [44,47]. Briefly, LNH is a measure of the alignment between velocity and vorticity vectors and is defined as:

$$\text{LNH}(\boldsymbol{x}) = \frac{\boldsymbol{v}(\boldsymbol{x}) \cdot \boldsymbol{\omega}(\boldsymbol{x})}{|\boldsymbol{v}(\boldsymbol{x})||\boldsymbol{\omega}(\boldsymbol{x})|} \tag{8}$$

where $\boldsymbol{v}$ and $\boldsymbol{\omega}$ are velocity and vorticity vectors, respectively. A quantitative description of helical flow was provided considering two helicity-based descriptors [46], namely the volume-average helicity intensity (h_2), and the unsigned balance of counter-rotating helical structures (h_4), derived in steady-state form as:

$$h_2 = \frac{1}{V}\int_V |\boldsymbol{v}(\boldsymbol{x}) \cdot \boldsymbol{\omega}(\boldsymbol{x})|\,\text{dV} \tag{9}$$

$$h_4 = \frac{\left|\int_V \boldsymbol{v}(\boldsymbol{x}) \cdot \boldsymbol{\omega}(\boldsymbol{x})\,\text{dV}\right|}{\int_V |\boldsymbol{v}(\boldsymbol{x}) \cdot \boldsymbol{\omega}(\boldsymbol{x})|\,\text{dV}} \qquad 0 \leq h_4 \leq 1 \tag{10}$$

where V is the integration volume. h_4 measures the strength of relative rotation of helical fluid structures in the fluid domain. It is a non-dimensional quantity ranging between 0 and 1: its value

10

equals 1 when only left-handed or right-handed helical structures are present in the integration volume and it is equal to 0 in case of reflectional symmetry. Four volumes of integration were defined, namely the whole main vessel, the volume of the proximal, mid and distal segments, following the same approach adopted for the computation of AWSS.

3. Results

3.1. Near-wall hemodynamics

The impact that the shape of the inflow velocity profile has on WSS was firstly evaluated in terms of AWSS percentage differences with respect to the reference (TP-only parabolic) velocity profile. In the box plot of Figure 3, the analysis is presented aggregating AWSS data from all the 10 LAD models on the basis of the specific velocity profile used as inflow boundary condition and considering the whole vessel and its division in three segments. Overall, the largest percentage differences from the reference TP-only parabolic velocity profile were observed in the proximal segment (median values range = [1.76%, 55.70%]), where they rose up to 100.24% in the case of the flat velocity profile (median value = 55.70%). The impact of the shape of the other inflow velocity profiles in the proximal segment was lower than 22.74% (velocity profile 1_2V_0.25 in geometry LAD8), with median value range = [1.76%, 5.71%] (Figure 3). In the mid segment, the maximum AWSS percentage differences from the reference case was reduced to 5.84% (velocity profile 1_2V_0.25 in geometry LAD8), with median value range = [0.01%, 0.96%] (Figure 3). AWSS percentage differences, came down to less than 1.00% in the distal segment, with a median value range = [0.00%, 0.77%] (Figure 3). Focusing on the whole vessel, the AWSS percentage differences from the reference (TP-only parabolic) velocity profile reflected the observed differences in the proximal LAD segment. In detail, the maximum percentage difference (16.70% for geometry LAD9) was observed for flat velocity profile, while for the other velocity profiles

percentage differences were lower than 5.81% (velocity profile 1_2V_0.25 in geometry LAD8), with a median value range = [0.34%, 1.67%]. Single cases percentage difference values are detailed in Table S1 of the Supplementary Material. For the sake of completeness, it is also reported that statistically significant differences in AWSS values emerged only in the proximal segment, and only between the reference (TP-only parabolic) velocity profile and the flat one (p-value<0.001, non-parametric Kruskal-Wallis test).

The impact of the shape inflow velocity profile on the distribution of the |WSS| on the LAD luminal surface can be appreciated by visual inspection of Figure 4, where the contour maps of the local percentage difference with respect to the reference (TP-only parabolic) velocity profile are displayed for two explanatory models, LAD7 and LAD8, presenting, respectively, the lowest and the highest maximum AWSS percentage difference, between the reference (TP-only parabolic) and the other velocity profiles (excluding the flat one) in the whole main vessel. The highest percentage differences from the reference WSS magnitude distribution were always located in the proximal segment. High differences (>100.00%) were observed also in the region of the first bifurcation only for model LAD8. However, this effect of the shape of the inflow velocity profile could be mainly ascribed to the fact that WSS magnitude values were lower than 0.5 Pa in a large part of this area (Figure 4), so that very small variations could give rise to high percentage differences. The |WSS| distribution on the luminal surface of the ten LAD models are presented in Figure S1 of the Supplementary Material.

The length of influence of the shape of the inflow velocity profile on near-wall hemodynamics, evaluated both in terms of maximum impact length and theoretical entrance length (Table 1), is visualized over each LAD model in Figure 5. It emerges that the theoretical entrance length evaluated using eq. (7) was always longer than the maximum impact length

(with the only exception of model LAD1). Therefore, the effects of the shape of the inflow velocity

profile on the average WSS magnitude over each vessel cross-section vanished within a few

diameters, and within a distance that was shorter than the one predicted by the theory in straight

cylindrical conduits (Figure 5).

3.2. Intravascular hemodynamics

The impact of the shape of the inflow velocity profile on intravascular flow was quantified

in terms of helicity intensity h_2 and counter-rotating helical patterns balance h_4. Their values,

integrated over each one of the ten LAD models main vessel, are presented in Figure 6. As a

general, observations, expectedly (1) the three-dimensionality of the inflow velocity profile (i.e.

the presence of an IP velocity component) was associated with higher h_2 values in the vessel,

while (2) counter-rotating helical structures were markedly unbalanced (higher h_4) when a

single-vortex IP velocity component was present in the imposed inflow velocity profile.

Here the impact of the shape of the inflow velocity profile was firstly evaluated in terms of

h_2 percentage difference and h_4 absolute difference with respect to the reference (TP-only

parabolic) velocity profile. In Figure 7, the analysis is presented aggregating h_2 and h_4 data from

all the 10 LAD models on the basis of the specific velocity profile used as inflow boundary

condition and considering the whole vessel and its division in three segments.

Also for helical flow, the largest differences from the reference (TP-only parabolic)

velocity profile for h_2 (maximum percentage difference of 602.27% profile 1_1V_-0.25 in

geometry LAD5; median values range = [20.72%, 292.79%]) and for h_4 (maximum absolute

difference of 0.93 profile 0_1V_-0.25 in geometry LAD3; median values range = [0.01, 0.87]) were

observed in the proximal segment. In the mid segment, the maximum h_2 percentage differences

13

decreased to 17.28% (profile 1_1V_-0.25 in geometry LAD5) with a median values range = [0.49%, 7.58%], while h_4 maximum absolute difference was reduced to 0.35 (median values range = [0.00, 0.09]). In the distal segment, h_2 percentage differences became lower than 2.84% (median values range = [0.01%, 2.37%]), except for geometry LAD8, which presented differences up to 18.13% (velocity profile 0_2V_0.25). In the distal segment h_4 presented the smallest absolute differences from the case of the reference velocity profile, lower than 0.16 (observed in model LAD8, profile 0_1V_-0.25), and with median values lower than 0.001. As for the whole main vessel, h_2 and h_4 differences from the reference (TP-only parabolic) velocity profile reflected the observed differences in the proximal LAD segment. In detail, the h_2 percentage differences presented a median values range = [6.12%, 65.88%] and maximum percentage differences lower than 107.64% (model LAD5, velocity profile 1_1V_-0.25). Regarding h_4 absolute differences, a median values range = [0.003, 0.470] and a maximum value of 0.68 (profile 0_1V_0.25 in geometry LAD8) were observed. A case-by-case summary of the differences for the reference (TP-only parabolic) velocity profile is reported in Table S2 and Table S3 of the Supplementary Material. For the sake of completeness, it is also reported that statistically significant differences (p-value<0.001) in h_2 values emerged only in the proximal segment with all velocity profiles that present the IP component (except for 0_2V_0.25 velocity profile), while for h_4 statistically significant differences (p-value<0.001) emerged in the proximal segment and in the whole main vessel, when velocity profiles with a single-vortex were imposed.

Finally, to better appreciate the impact of the shape of the inflow velocity profile on LAD intravascular flow, LNH isosurfaces are visualized in Figure 8. For the sake of synthesis, the cases characterized by the minimum and the maximum percentage difference in h_2 with respect to the reference parabolic velocity profile (LAD10 and LAD5, respectively) are reported in Figure 8,

while all geometries are shown in the Supplementary Material (Figure S2). The LNH-based visualization confirms that, in general, the presence of an IP component on the inflow velocity profile enriched helical flow in the LAD proximal segment. Moreover, the structure of the IP velocity component (i.e., single- or double-vortex shape) dictated the arrangement of helical flow patterns in one or two counter-rotating structures (cases denoted by 1V and 2V in Figure 8, respectively).

4. Discussion

In computational hemodynamics, when dealing with patient-specific models, the imposition of *in vivo* measured 3D velocity profiles as inflow boundary condition leads to more realistic simulations. However, velocity profiles are often not measurable *in vivo*, and their idealized versions, based upon assumptions needed to fill a gap of knowledge, are prescribed to model blood flow.

In coronary arteries, blood flow velocity values can be derived *in vivo* from Doppler flow velocity or thermodilution measurements [48,49]. Nevertheless, these techniques (1) are uncommon in the clinical practice, and (2) provide an estimation of blood velocity averaged over the vessel cross-section. Consequently, as information on the three components of the velocity profile is not available, idealized velocity profiles need to be assumed a priori to turn the defective boundary data problem into a classic Dirichlet problem. Such an assumption can influence the numerical solution, potentially weakening the findings of the *in silico* experiments. In this regard, the uncertainty associated with the use of idealized velocity profiles as inflow boundary condition in computational hemodynamics has been investigated in, e.g., carotid arteries [50,51] and ascending aorta [31,52,53], where 3D velocity profiles can be measured *in*

vivo, but not in coronary arteries.

Motivated by this, ten LAD geometries were reconstructed from two angiographic projections, using a new reconstruction method that allows obtaining multiple branches in the LAD geometries. To evaluate the impact of assumptions on the shape of the inflow velocity profiles on coronary hemodynamics, a novel framework to generate 3D velocity profiles on non-circular shaped blood vessels cross-sections was developed by generalizing analytical formulations. The impact of inflow velocity profiles was tested in terms of near-wall and intravascular physiologically relevant hemodynamic quantities.

Using the widely adopted inflow parabolic velocity profile as reference profile, here we found that, in terms of AWSS, all the investigated cases present percentage differences <5.80%, except for the flat velocity profile, presenting differences up to 16.70%. The highest percentage differences were observed in the proximal segment of the vessel models, while moderate-to-negligible differences were observed in mid and distal segments (Figure 3). These findings are consistent with those previously observed in a simplified computational model of right coronary artery [54] when comparing idealized, only TP flat, parabolic and Dean-like inflow velocity profiles. Also in that study, the impact of the velocity profile on WSS was limited to the proximal part of vessel [54].

As expected, it emerged that the presence of secondary flow (IP) component in the inflow velocity profile has a marked impact on helical flow. Such marked differences, dictated by the shape of the inflow velocity profile, are mainly located in the proximal segment (up to 602.27%), where the imposition of TP-only velocity profiles leads to a production of helicity intensity h_2 smaller than 3D velocity profiles. In the mid and distal segments, maximum differences in helical flow intensity decreases to values lower than 18.13% confirming the main role played by

16

geometry in the dispersal of the imposed inlet velocity profile and in the production/disruption of laminar helicity intensity [38]. The impact that the presence of IP components in the inflow velocity profiles has on helical flow patterns downstream configuration emerges also by the analysis of h_4, highlighting how the presence of one main or two balanced counter-rotating helical flow patterns in the proximal segment is dictated by the single- or double-vortex shape of the IP component of the inflow velocity profile. Interestingly, in the proximal segment h_4 values in the TP-only velocity profiles are low, suggesting that the production of almost balanced counter-rotating bi-helical blood flow patterns is dictated by the arterial geometry. Moreover, as a consequence of a double-vortex IP configuration at the inlet the bi-helical flow patterns in the proximal segment are almost balanced by construction and therefore present low h_4 values (as in the TP-only velocity profile cases). On the opposite, in the case of inflow velocity profiles with single-vortex IP component h_4 values are close to 1 indicating that one helical direction of rotation predominates in the flow field. In the mid and distal coronary segments, the impact of the presence of IP components in the imposed inflow velocity profile on helical structures balance vanishes, and vessel geometry mainly dictates blood flow arrangement in helical patterns.

Overall, the findings of this study suggest that the influence of the shape of the velocity profile imposed at the inflow section in computational hemodynamics models of LAD coronary arteries is limited to few diameters downstream. Taking into consideration the importance of the entrance length, also highlighted elsewhere [54], a more realistic hemodynamic picture in proximal LAD coronary arteries could be obtained extending the reconstruction upstream, including the left main coronary artery or even the aortic root. However, the advantage coming from the reconstruction of the geometry up to the aortic root, which assures a minor dependence

17

of the proximal LAD simulated hemodynamics on inflow boundary conditions, cannot be exploited using the here adopted, routine invasive coronary angiography, which is the most convenient clinical modality [55].

This study presents limitations that might weaken the current findings. The lack of the real, *in vivo* measured 3D velocity profiles in the LAD enforced the generation of velocity profiles (1) based upon analytical formulations, and (2) with an arbitrary amount of secondary flows, deemed as representative of the real situation. However, the proposed approach has the advantage of generating velocity profiles in a tightly controlled manner, allowing to test differently shaped inflow velocity patterns. Moreover, steady-state simulations were carried out, neglecting the pulsatile nature of coronary flow. This choice was based on previous computational studies demonstrating that for flow regimes characterized by low Reynolds numbers, like those of coronary arteries, the difference between time averaged **WSS** and the steady-state |**WSS**| is negligible [56,57]. It is also worth noting that the steady flow assumption reduced sensibly the computational cost, given reliable results meeting clinical time constraints. Lastly, the idealization of velocity profiles as inflow boundary condition in LAD coronary arteries represents just one source of uncertainty that nonlinearly pile-up with other uncertainties regarding: (1) the flow rate estimation [39]; (2) the assumption of rigid wall [58], even if recent findings suggest a negligible impact of wall deformability on WSS in coronary arteries [59]; (3) the cardiac motion and coronary displacement, here not considered even if not univocal conclusions are reported [60,61]. All these assumptions could affect the results. However, here we focused on a single source of uncertainty to link the observed differences to unambiguous causes.

18

5. Conclusions

In this study, the impact of the shape of blood velocity profiles, prescribed as inflow boundary conditions in image-based computational models of LAD coronary arteries, on local hemodynamics was evaluated. Our findings highlighted that the hemodynamic impact of considering realistic 3D features, such as eccentricity and differently shaped secondary flows, as a part of the inflow velocity profile is limited to the proximal LAD segment. Furthermore, the findings suggested that the problem of the paucity of information affecting the imposition of as realistic as possible velocity profiles as inflow boundary condition in LAD models can be satisfactorily overcome by applying idealized inflow parabolic velocity profiles, as long as the proximal LAD segment is not considered in the evaluation of the results. As a pragmatic rule of thumb, a conservative estimation of the length of influence of the shape of the inflow velocity profile on LAD local hemodynamics can be given by the theoretical entrance length, in general longer than the maximum impact length.

The strategy proposed here to manage inflow boundary conditions, which emerged studying healthy, image-based LAD models, may be translated to diseased or stented coronary vessels, given that the reconstructed coronary artery geometry upstream of the lesion or of the stent is sufficiently extended.

Conflict of interest

The authors have no professional or financial conflicts of interest to disclose.

References

[1]   Boudoulas KD, Triposciadis F, Geleris P, Boudoulas H. Coronary Atherosclerosis: Pathophysiologic Basis for Diagnosis and Management. Prog Cardiovasc Dis 2016;58:676–92. https://doi.org/10.1016/j.pcad.2016.04.003.

[2]   Antoniadis AP, Giannopoulos AA, Wentzel JJ, Joner M, Giannoglou GD, Virmani R, et al. Impact of local flow haemodynamics on atherosclerosis in coronary artery bifurcations. EuroIntervention 2015;11:V18–22. https://doi.org/10.4244/EIJV11SVA4.

[3]   Malek AM, Alper SL, Izumo S. Hemodynamic Shear Stress and Its Role in Atherosclerosis. JAMA 1999;282:2035–42. https://doi.org/10.1001/jama.282.21.2035.

[4]   Morbiducci U, Kok AM, Kwak BR, Stone PH, Steinman DA, Wentzel JJ. Atherosclerosis at arterial bifurcations: Evidence for the role of haemodynamics and geometry. Thromb Haemost 2016;115:484–92. https://doi.org/10.1160/TH15-07-0597.

[5]   Samady H, Eshtehardi P, McDaniel MC, Suo J, Dhawan SS, Maynard C, et al. Coronary artery wall shear stress is associated with progression and transformation of atherosclerotic plaque and arterial remodeling in patients with coronary artery disease. Circulation 2011;124:779–88. https://doi.org/10.1161/CIRCULATIONAHA.111.021824.

[6]   Wentzel JJ, Chatzizisis YS, Gijsen FJH, Giannoglou GD, Feldman CL, Stone PH. Endothelial shear stress in the evolution of coronary atherosclerotic plaque and vascular remodelling: Current understanding and remaining questions. Cardiovasc Res 2012;96:234–43. https://doi.org/10.1093/cvr/cvs217.

[7]   Kwak BR, Bäck M, Bochaton-Piallat ML, Caligiuri G, Daemen MJAP, Davies PF, et al. Biomechanical factors in atherosclerosis: Mechanisms and clinical implications. Eur Heart J 2014;35:3013–20. https://doi.org/10.1093/eurheartj/ehu353.

[8]   Hoogendoorn A, Kok AM, Hartman EMJ, de Nisco G, Casadonte L, Chiastra C, et al. Multidirectional wall shear stress promotes advanced coronary plaque development: comparing five shear stress metrics. Cardiovasc Res 2019. https://doi.org/10.1093/cvr/cvz212.

[9]   De Nisco G, Kok AM, Chiastra C, Gallo D, Hoogendoorn A, Migliavacca F, et al. The Atheroprotective Nature of Helical Flow in Coronary Arteries. Ann Biomed Eng 2019;47:425–38. https://doi.org/10.1007/s10439-018-02169-x.

[10]   De Nisco G, Hoogendoorn A, Chiastra C, Gallo D, Kok AM, Morbiducci U, et al. The impact of helical flow on coronary atherosclerotic plaque development. Atherosclerosis 2020. https://doi.org/10.1016/J.ATHEROSCLEROSIS.2020.01.027.

[11]   Taylor CA, Steinman DA. Image-based modeling of blood flow and vessel wall dynamics: Applications, methods and future directions: Sixth international bio-fluid mechanics symposium and workshop, March 28-30, 2008 Pasadena, California. Ann Biomed Eng 2010;38:1188–203. https://doi.org/10.1007/s10439-010-9901-0.

[12]   Morris PD, Narracott A, Von Tengg-Kobligk H, Soto DAS, Hsiao S, Lungu A, et al. Computational fluid dynamics modelling in cardiovascular medicine. Heart 2016;102:18–28. https://doi.org/10.1136/heartjnl-2015-308044.

[13]   Zhong L, Zhang JM, Su B, Tan RS, Allen JC, Kassab GS. Application of patient-specific computational fluid dynamics in coronary and intra-cardiac flow simulations: Challenges and opportunities. Front Physiol 2018;9. https://doi.org/10.3389/fphys.2018.00742.

[14]   Sankaran S, Kim HJ, Choi G, Taylor CA. Uncertainty quantification in coronary blood flow simulations: Impact of geometry, boundary conditions and blood viscosity. J Biomech 2016;49:2540–7. https://doi.org/10.1016/j.jbiomech.2016.01.002.

[15]   Bozzi S, Morbiducci U, Gallo D, Ponzini R, Rizzo G, Bignardi C, et al. Uncertainty propagation of phase contrast-MRI derived inlet boundary conditions in computational hemodynamics models of thoracic aorta. Comput Methods Biomech Biomed Engin 2017;20:1104–12. https://doi.org/10.1080/10255842.2017.1334770.

[16]   Steinman DA, Migliavacca F. Editorial: Special Issue on Verification, Validation, and Uncertainty Quantification of Cardiovascular Models: Towards Effective VVUQ for Translating Cardiovascular Modelling to Clinical Utility. Cardiovasc Eng Technol 2018;9:539–43. https://doi.org/10.1007/s13239-018-00393-z.

[17]   Boccadifuoco A, Mariotti A, Capellini K, Celi S, Salvetti MV. Validation of Numerical Simulations of Thoracic Aorta Hemodynamics: Comparison with In Vivo Measurements and Stochastic Sensitivity Analysis. Cardiovasc Eng Technol 2018;9:688–706. https://doi.org/10.1007/s13239-018-00387-x.

[18]   Boccadifuoco A, Mariotti A, Celi S, Martini N, Salvetti M V. Impact of uncertainties in outflow boundary conditions on the predictions of hemodynamic simulations of ascending thoracic aortic aneurysms. Comput Fluids 2018;165:96–115. https://doi.org/https://doi.org/10.1016/j.compfluid.2018.01.012.

[19]   Hose DR, Lawford P V., Huberts W, Hellevik LR, Omholt SW, van de Vosse FN. Cardiovascular models for personalised medicine: Where now and where next? Med Eng Phys 2019;72:38–48. https://doi.org/10.1016/j.medengphy.2019.08.007.

[20]   Antonuccio MN, Mariotti A, Celi S, Salvetti MV. Effects of the Distribution in Space of the Velocity-Inlet Condition in Hemodynamic Simulations of the Thoracic Aorta BT - Bioinformatics and Biomedical Engineering. In: Rojas I, Valenzuela O, Rojas F, Herrera LJ, Ortuño F, editors., Cham: Springer International Publishing; 2020, p. 63–74.

[21] Markl M, Schnell S, Wu C, Bollache E, Jarvis K, Barker AJ, et al. Advanced flow MRI: emerging techniques and applications. Clin Radiol 2016. https://doi.org/10.1016/j.crad.2016.01.011.

[22] Giannopoulos AA, Chatzizisis YS, Maurovich-Horvat P, Antoniadis AP, Hoffmann U, Steigner ML, et al. Quantifying the effect of side branches in endothelial shear stress estimates. Atherosclerosis 2016;251:213–8. https://doi.org/10.1016/j.atherosclerosis.2016.06.038.

[23] Vorobtsova N, Chiastra C, Stremler MA, Sane DC, Migliavacca F, Vlachos P. Effects of Vessel Tortuosity on Coronary Hemodynamics: An Idealized and Patient-Specific Computational Study. Ann Biomed Eng 2016;44:2228–39. https://doi.org/10.1007/s10439-015-1492-3.

[24] Kumar A, Hung OY, Piccinelli M, Eshtehardi P, Corban MT, Sternheim D, et al. Low Coronary Wall Shear Stress Is Associated With Severe Endothelial Dysfunction in Patients With Nonobstructive Coronary Artery Disease. JACC Cardiovasc Interv 2018;11:2072–80. https://doi.org/10.1016/j.jcin.2018.07.004.

[25] Bologna M, Migliori S, Montin E, Rampat R, Dubini G, Migliavacca F, et al. Automatic segmentation of optical coherence tomography pullbacks of coronary arteries treated with bioresorbable vascular scaffolds: Application to hemodynamics modeling. PLoS One 2019;14:1–17. https://doi.org/10.1371/journal.pone.0213603.

[26] Chiastra C, Morlacchi S, Gallo D, Morbiducci U, Cárdenes R, Larrabide I, et al. Computational fluid dynamic simulations of image-based stented coronary bifurcation models. J R Soc Interface 2013;10. https://doi.org/10.1098/rsif.2013.0193.

[27] Beier S, Ormiston J, Webster M, Cater J, Norris S, Medrano-Gracia P, et al. Impact of bifurcation angle and other anatomical characteristics on blood flow - A computational study of non-stented and stented coronary arteries. J Biomech 2016;49:1570–82.

https://doi.org/10.1016/j.jbiomech.2016.03.038.

[28]   Doutel E, Pinto SIS, Campos JBLM, Miranda JM. Link between deviations from Murray's Law
          and occurrence of low wall shear stress regions in the left coronary artery. J Theor Biol
          2016;402:89–99. https://doi.org/10.1016/j.jtbi.2016.04.038.

[29]   Pinto SIS, Campos JBLM. Numerical study of wall shear stress-based descriptors in the
          human left coronary artery. Comput Methods Biomech Biomed Engin 2016;19:1443–55.
          https://doi.org/10.1080/10255842.2016.1149575.

[30]   Migliori S, Chiastra C, Bologna M, Montin E, Dubini G, Genuardi L, et al. Application of an
          OCT-based 3D reconstruction framework to the hemodynamic assessment of an ulcerated
          coronary artery plaque. Med Eng Phys 2020.
          https://doi.org/10.1016/j.medengphy.2019.12.006.

[31]   Morbiducci U, Ponzini R, Gallo D, Bignardi C, Rizzo G. Inflow boundary conditions for
          image-based computational hemodynamics: Impact of idealized versus measured velocity
          profiles in the human aorta. J Biomech 2013;46:102–9.
          https://doi.org/10.1016/j.jbiomech.2012.10.012.

[32]   Beier S, Ormiston JA, Webster MW, Cater JE, Norris SE, Medrano-Gracia P, et al.
          Dynamically scaled phantom phase contrast MRI compared to true-scale computational
          modeling of coronary artery flow. J Magn Reson Imaging 2016;44:983–92.
          https://doi.org/10.1002/jmri.25240.

[33]   Bahrami S, Norouzi M. A numerical study on hemodynamics in the left coronary bifurcation
          with normal and hypertension conditions. Biomech Model Mechanobiol 2018;17:1785–96.
          https://doi.org/10.1007/s10237-018-1056-1.

[34]   Doutel E, Carneiro J, Campos JBLM, Miranda JM. Experimental and numerical methodology

to analyze flows in a coronary bifurcation. Eur J Mech B/Fluids 2018;67:341–56.

https://doi.org/10.1016/j.euromechflu.2017.09.009.

[35] Wellnhofer E, Osman J, Kertzscher U, Affeld K, Fleck E, Goubergrits L. Flow simulation

studies in coronary arteries-Impact of side-branches. Atherosclerosis 2010;213:475–81.

https://doi.org/10.1016/j.atherosclerosis.2010.09.007.

[36] Li Y, Gutiérrez-Chico JL, Holm NR, Yang W, Hebsgaard L, Christiansen EH, et al. Impact of

Side Branch Modeling on Computation of Endothelial Shear Stress in Coronary Artery

Disease: Coronary Tree Reconstruction by Fusion of 3D Angiography and OCT. J Am Coll

Cardiol 2015;66:125–35. https://doi.org/10.1016/j.jacc.2015.05.008.

[37] Vardhan M, Gounley J, Chen SJ, Kahn AM, Leopold JA, Randles A. The importance of side

branches in modeling 3D hemodynamics from angiograms for patients with coronary

artery disease. Sci Rep 2019;9:1–10. https://doi.org/10.1038/s41598-019-45342-5.

[38] Chiastra C, Gallo D, Tasso P, Iannaccone F, Migliavacca F, Wentzel JJ, et al. Healthy and

diseased coronary bifurcation geometries influence near-wall and intravascular flow: A

computational exploration of the hemodynamic risk. J Biomech 2017;58:79–88.

https://doi.org/10.1016/j.jbiomech.2017.04.016.

[39] van der Giessen AG, Groen HC, Doriot PA, de Feyter PJ, van der Steen AFW, van de Vosse

FN, et al. The influence of boundary conditions on wall shear stress distribution in patients

specific coronary trees. J Biomech 2011;44:1089–95.

https://doi.org/10.1016/j.jbiomech.2011.01.036.

[40] Zovatto L, Pedrizzetti G. Optimal helical entry flow in a helical vessel. Fluid Dyn Res

2018;50. https://doi.org/10.1088/1873-7005/aadefd.

[41] Dean WR. XVI. Note on the motion of fluid in a curved pipe. London, Edinburgh, Dublin

Philos Mag J Sci 1927;4:208–23. https://doi.org/10.1080/14786440708564324.

[42]   WG Austen , JE Edwards , RL Frye , GG Gensini , VL Gott , LS Griffith , DC McGoon , ML
       Murphy BR. AHA COMMITTEE REPORT: A Reporting System on Patients Evaluated for
       Coronary Artery Disease Report of the Ad Hoc Committee for Grading of Coronary Artery.
       Circulation 1975;51:5–40.

[43]   Bergman TL, Incropera FP, DeWitt DP, Lavine AS. Fundamentals of Heat and Mass Transfer.
       Wiley; 2011.

[44]   Morbiducci U, Ponzini R, Grigioni M, Redaelli A. Helical flow as fluid dynamic signature for
       atherogenesis risk in aortocoronary bypass. A numeric study. J Biomech 2007;40:519–34.
       https://doi.org/10.1016/j.jbiomech.2006.02.017.

[45]   Morbiducci U, Ponzini R, Rizzo G, Cadioli M, Esposito A, Montevecchi FM, et al. Mechanistic
       insight into the physiological relevance of helical blood flow in the human aorta: An in vivo
       study. Biomech Model Mechanobiol 2011;10:339–55. https://doi.org/10.1007/s10237-
       010-0238-2.

[46]   Gallo D, Steinman DA, Bijari PB, Morbiducci U. Helical flow in carotid bifurcation as
       surrogate marker of exposure to disturbed shear. J Biomech 2012;45:2398–404.
       https://doi.org/10.1016/j.jbiomech.2012.07.007.

[47]   Shtilman L, Levich E, Orszag SA, Pelz RB, Tsinober A. On the role of helicity in complex fluid
       flows. Phys Lett A 1985;113:32–7. https://doi.org/10.1016/0375-9601(85)90600-0.

[48]   Everaars H, de Waard GA, Driessen RS, Danad I, van de Ven PM, Raijmakers PG, et al.
       Doppler Flow Velocity and Thermodilution to Assess Coronary Flow Reserve: A Head-to-
       Head Comparison With [15O]H2O PET. JACC Cardiovasc Interv 2018;11:2044–54.
       https://doi.org/10.1016/j.jcin.2018.07.011.

[49] Xaplanteris P, Fournier S, Keulards DCJ, Adjedj J, Ciccarelli G, Milkas A, et al. Catheter-based measurements of absolute coronary blood flow and microvascular resistance feasibility, safety, and reproducibility in humans. Circ Cardiovasc Interv 2018;11:1–8. https://doi.org/10.1161/CIRCINTERVENTIONS.117.006194.

[50] Wake AK, Oshinski JN, Tannenbaum AR, Giddens DP. Choice of in vivo versus idealized velocity boundary conditions influences physiologically relevant flow patterns in a subject-specific simulation of flow in the human carotid bifurcation. J Biomech Eng 2009;131:7–13. https://doi.org/10.1115/1.3005157.

[51] Campbell IC, Ries J, Dhawan SS, Quyyumi AA, Taylor WR, Oshinski JN. Effect of inlet velocity profiles on patient-specific computational fluid dynamics simulations of the carotid bifurcation. J Biomech Eng 2012;134:1–8. https://doi.org/10.1115/1.4006681.

[52] Pirola S, Jarral OA, O'Regan DP, Asimakopoulos G, Anderson JR, Pepper JR, et al. Computational study of aortic hemodynamics for patients with an abnormal aortic valve: The importance of secondary flow at the ascending aorta inlet. APL Bioeng 2018;2:026101. https://doi.org/10.1063/1.5011960.

[53] Youssefi P, Gomez A, Arthurs C, Sharma R, Jahangiri M, Figueroa CA. Impact of patient-specific inflow velocity profile on hemodynamics of the thoracic aorta. J Biomech Eng 2018;140:1–14. https://doi.org/10.1115/1.4037857.

[54] Myers JG, Moore JA, Ojha M, Johnston KW, Ethier CR. Factors influencing blood flow patterns in the human right coronary artery. Ann Biomed Eng 2001;29:109–20. https://doi.org/10.1114/1.1349703.

[55] Collet C, Onuma Y, Andreini D, Sonck J, Pompilio G, Mushtaq S, et al. Coronary computed tomography angiography for heart team decision-making in multivessel coronary artery

disease. Eur Heart J 2018;39:3689–98. https://doi.org/10.1093/eurheartj/ehy581.

[56]   Pedley TJ. The Fluid Mechanics of Large Blood Vessels. Cambridge: Cambridge University Press; 1980. https://doi.org/DOI: 10.1017/CBO9780511896996.

[57]   Kumar A, Thompson EW, Lefieux A, Molony DS, Davis EL, Chand N, et al. High Coronary Shear Stress in Patients With Coronary Artery Disease Predicts Myocardial Infarction. J Am Coll Cardiol 2018;72:1926–35. https://doi.org/10.1016/j.jacc.2018.07.075.

[58]   Malvè M, García A, Ohayon J, Martínez MA. Unsteady blood flow and mass transfer of a human left coronary artery bifurcation: FSI vs. CFD. Int Commun Heat Mass Transf 2012;39:745–51. https://doi.org/10.1016/j.icheatmasstransfer.2012.04.009.

[59]   Eslami P, Tran J, Jin Z, Karady J, Sotoodeh R, Lu MT, et al. Effect of Wall Elasticity on Hemodynamics and Wall Shear Stress in Patient-Specific Simulations in the Coronary Arteries. J Biomech Eng 2020;142:1–10. https://doi.org/10.1115/1.4043722.

[60]   Theodorakakos A, Gavaises M, Andriotis A, Zifan A, Liatsis P, Pantos I, et al. Simulation of cardiac motion on non-Newtonian, pulsating flow development in the human left anterior descending coronary artery. Phys Med Biol 2008;53:4875–92. https://doi.org/10.1088/0031-9155/53/18/002.

[61]   Javadzadegan A, Yong ASC, Chang M, Ng MKC, Behnia M, Kritharides L. Haemodynamic assessment of human coronary arteries is affected by degree of freedom of artery movement. Comput Methods Biomech Biomed Engin 2017;20:260–72. https://doi.org/10.1080/10255842.2016.1215439.
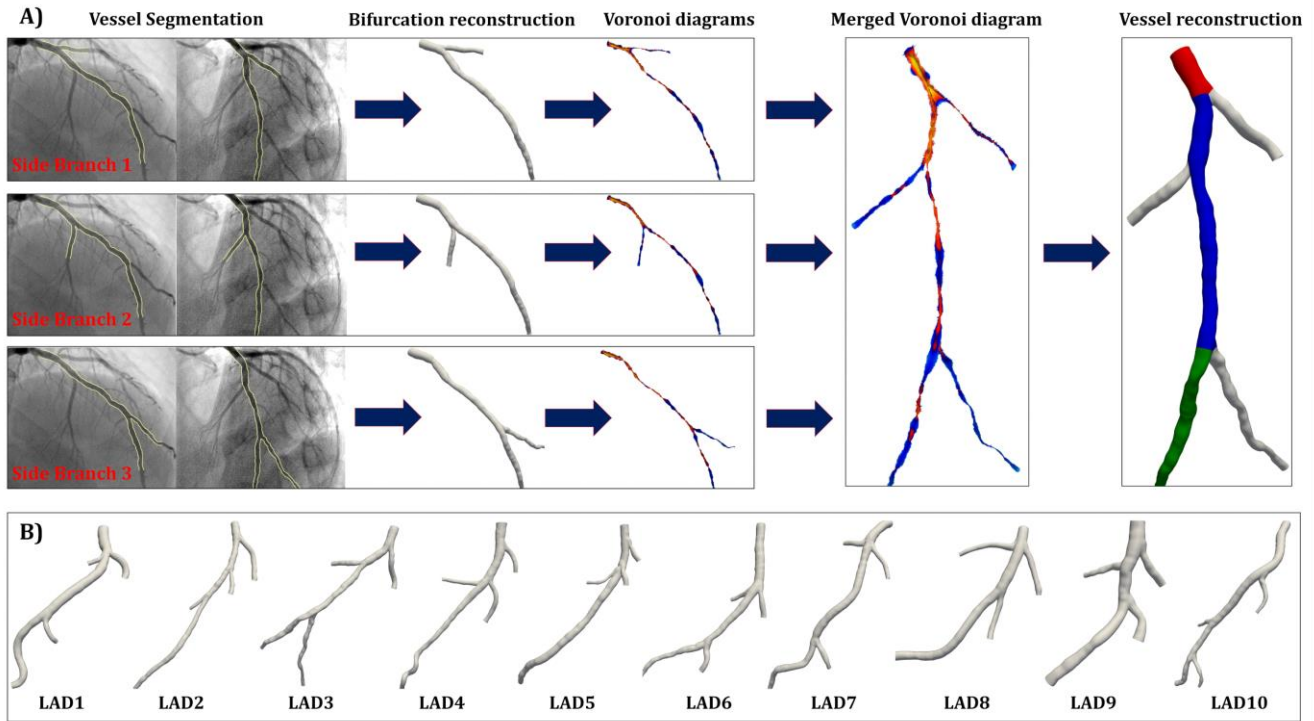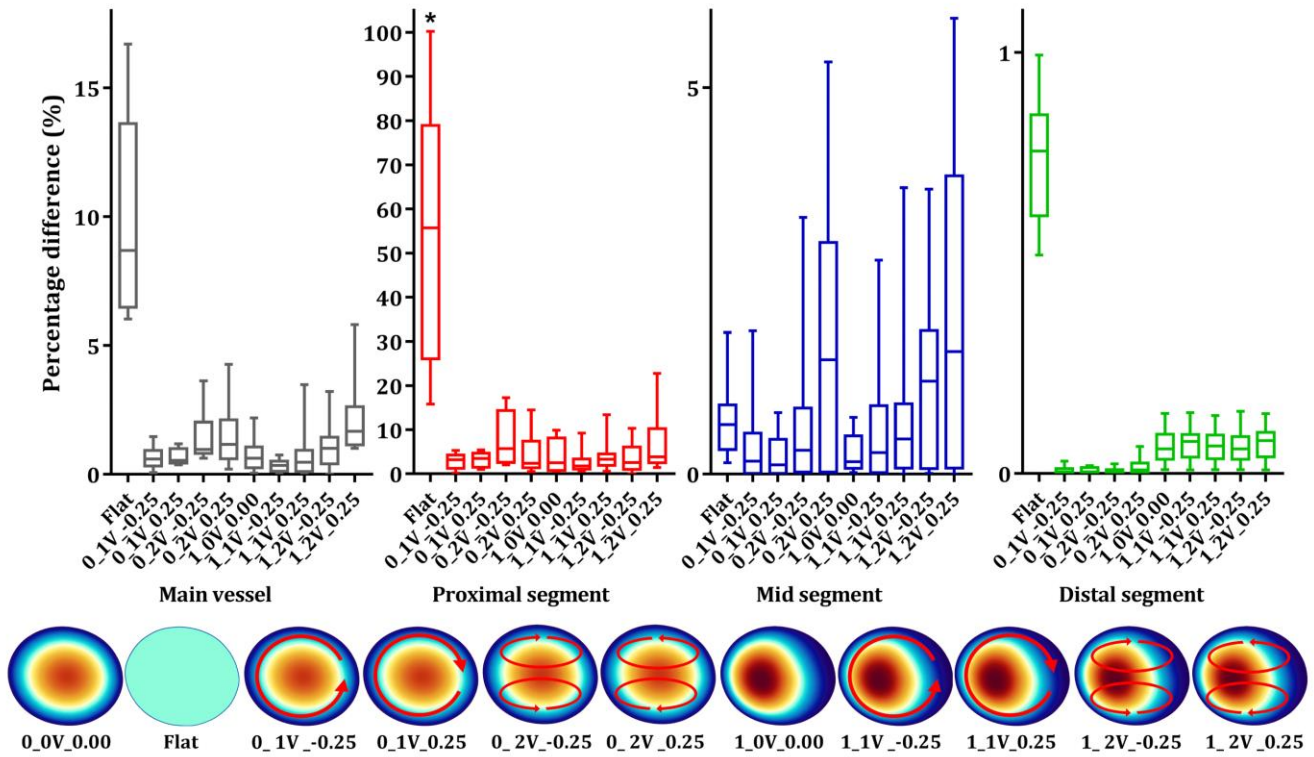
Figures

Figure 1. A) Workflow for the three-dimensional reconstruction of left anterior descending (LAD) coronary artery geometries from two angiographic projections. From left to right: single bifurcation segmentation, single bifurcation reconstruction, Voronoi diagrams computation, Voronoi diagrams merging, and geometry reconstruction. Proximal, mid and distal segments are colour coded (red, blue and green, respectively) according to American Heart Association classification. B) The ten reconstructed LAD coronary artery geometries.
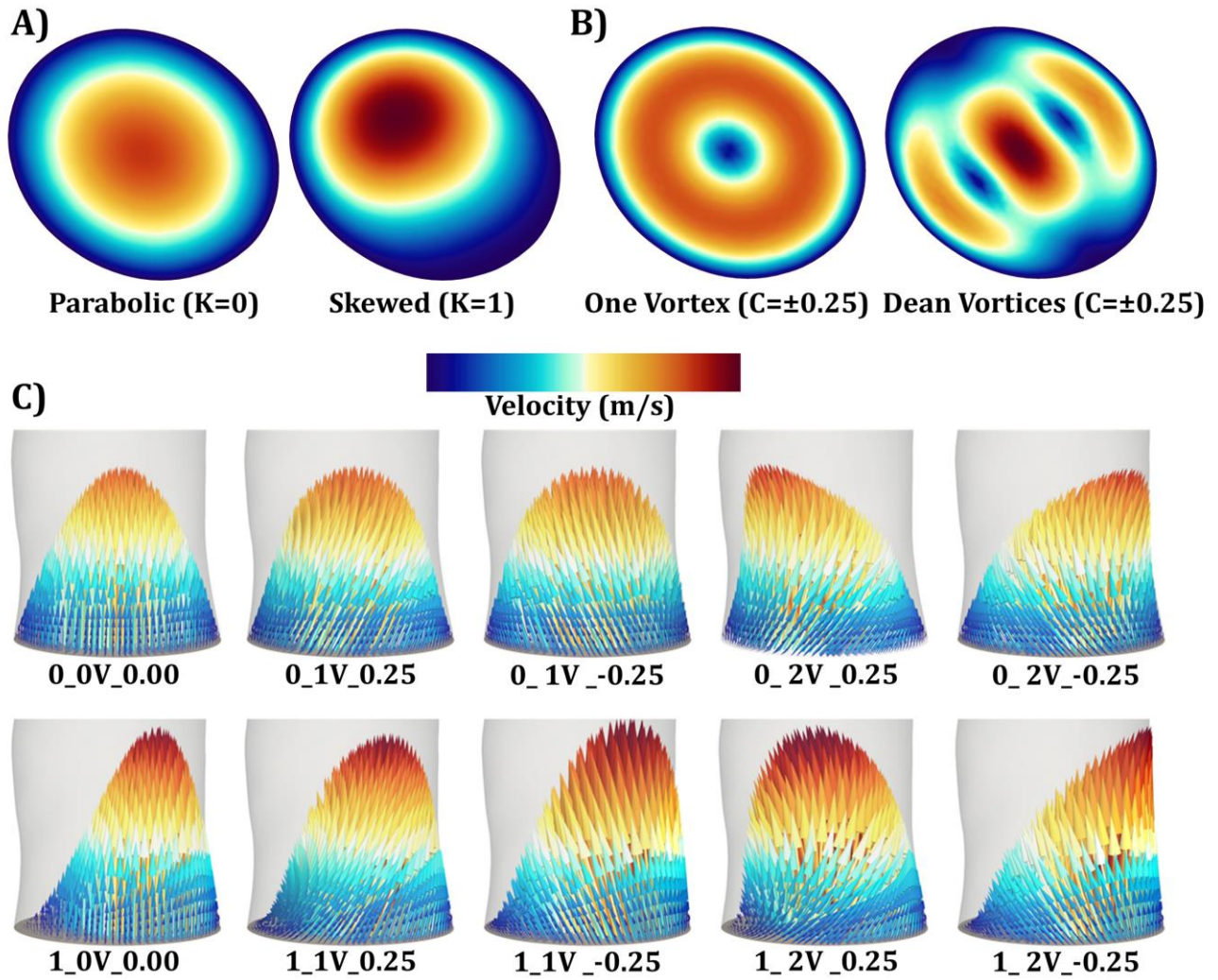
Figure 2. Generated velocity profiles: A) Colour maps of the through-plane (TP) velocity component coloured according to TP velocity magnitude; B) colour maps of the in-plane (IP) velocity component coloured according to IP velocity magnitude; C) three-dimensional velocity profile scaled vectors, coloured according to velocity magnitude.

Figure 3. From left to right: percentage differences of surface averaged |**WSS**| (AWSS) between the reference (0_0V_0.00) and the other velocity profiles in the main vessel, proximal, mid and distal segments. Statistically significant differences are indicated with * (p-value<0.001).
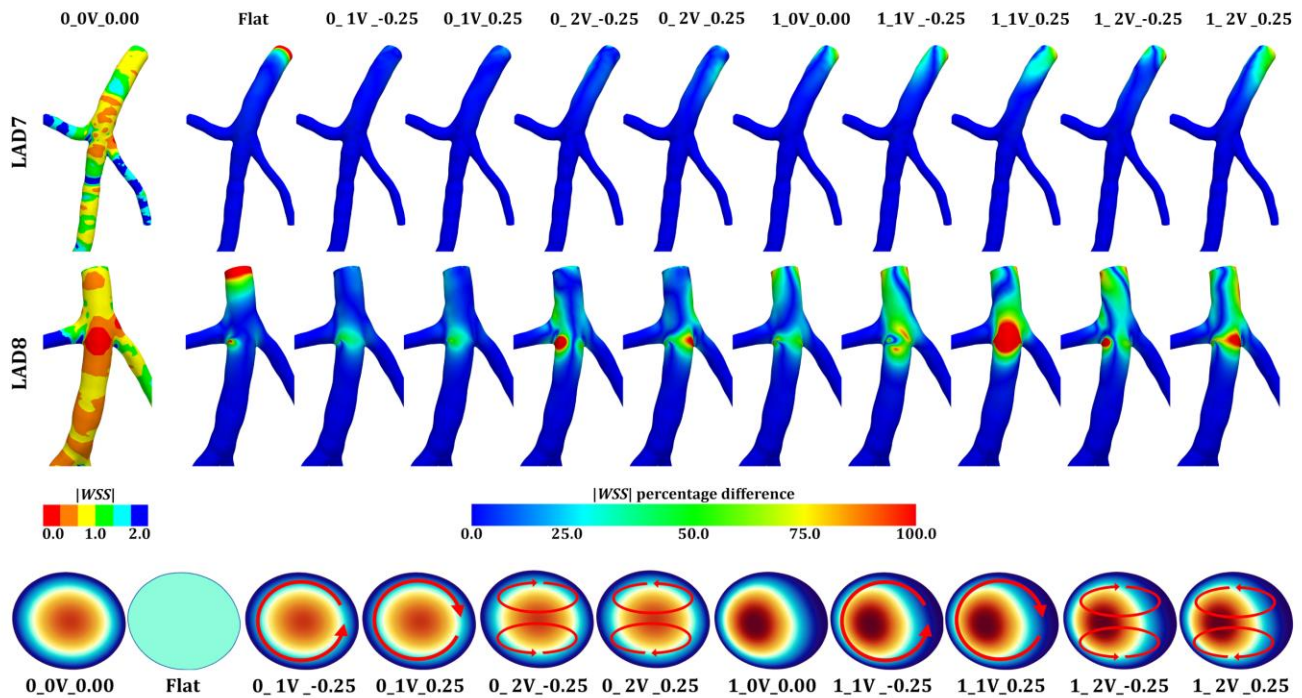
Figure 4. On the left: distribution of |**WSS**| at the luminal surface for the reference velocity profile (0_0V_0.00); on the right: distribution of |**WSS**| percentage differences between the reference and the other velocity profiles. Two explanatory case are reported (i.e. the models with the lowest and the highest AWSS difference in the main vessel, namely LAD7 and LAD8, respectively). A magnified view of the vessels is presented for a clearer visualization of the results.
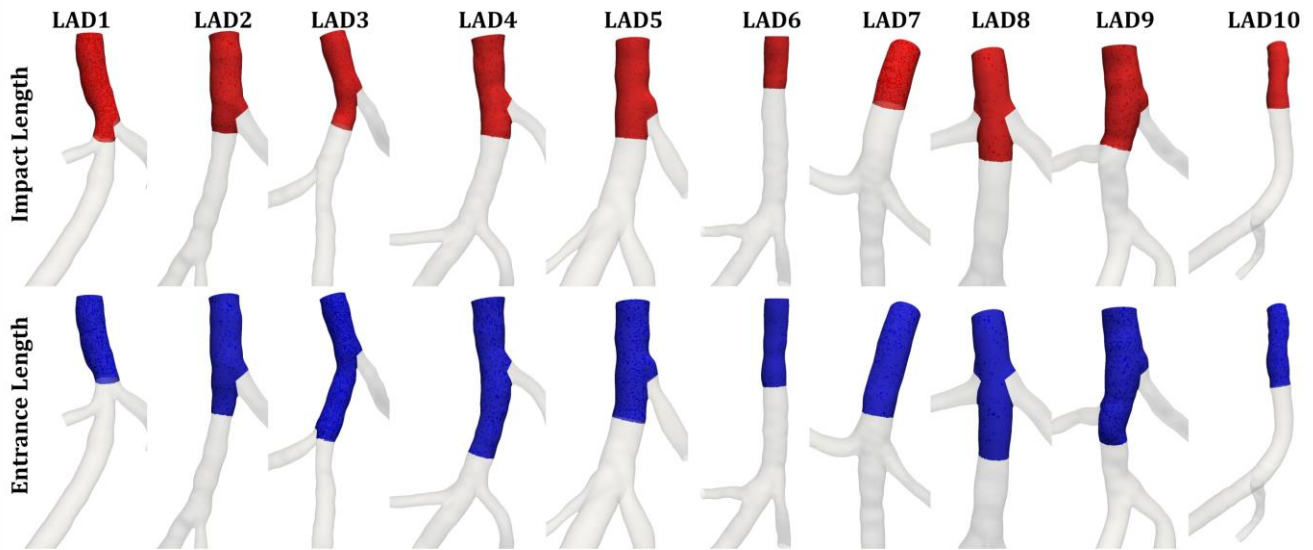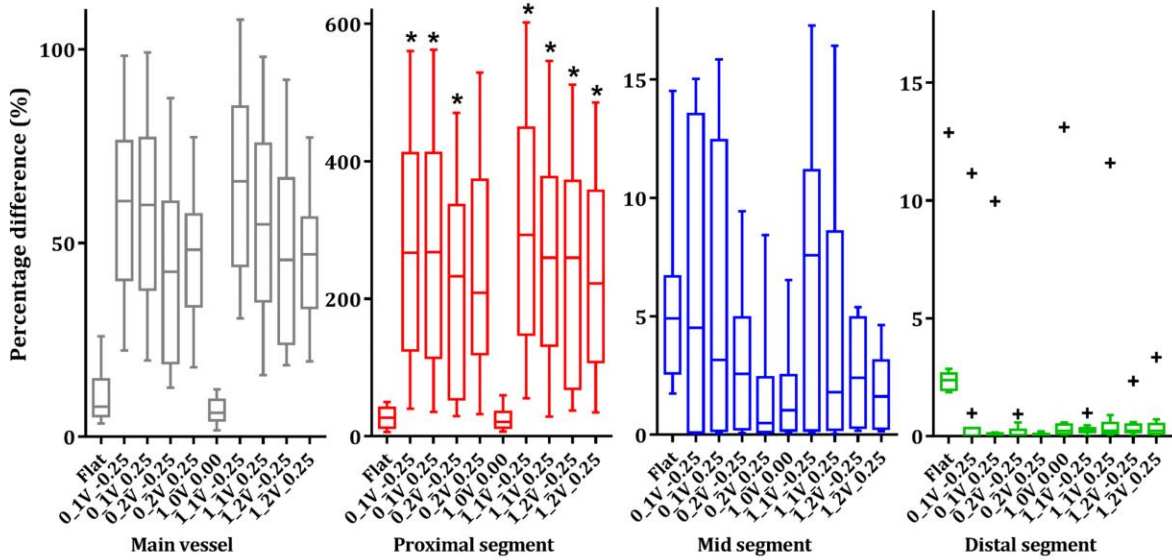
Figure 5. Upper panel: impact length is highlighted in red for each model. Lower panel: theoretical entrance length is highlighted in blue for each model. A magnified view of the vessels is presented for a clearer visualization of the results.
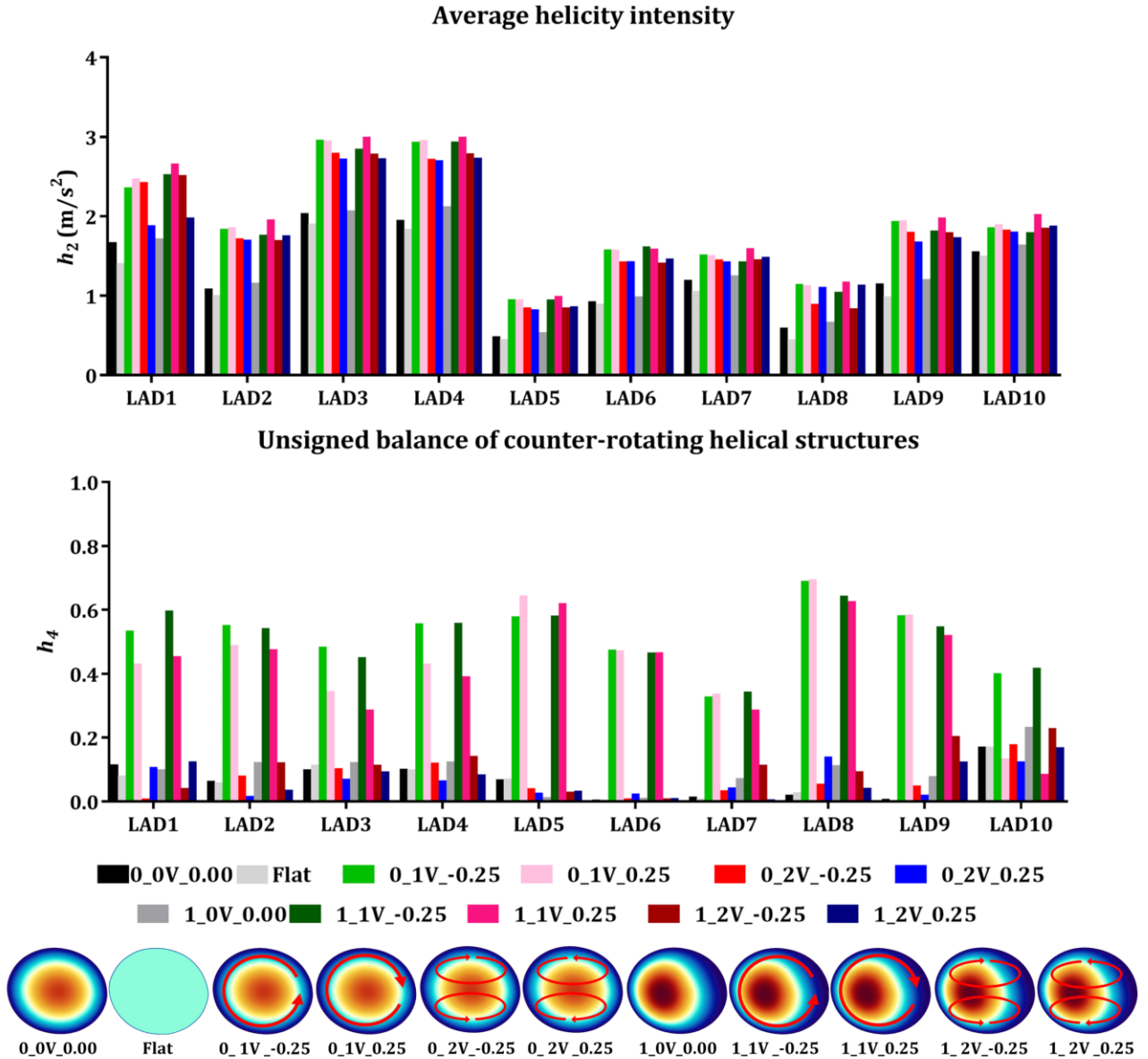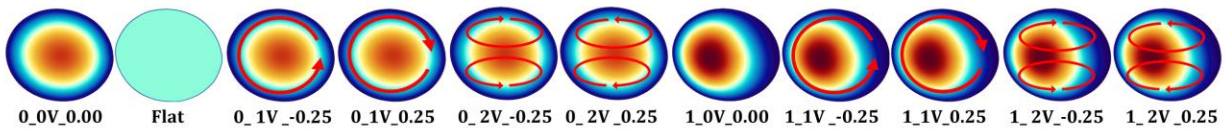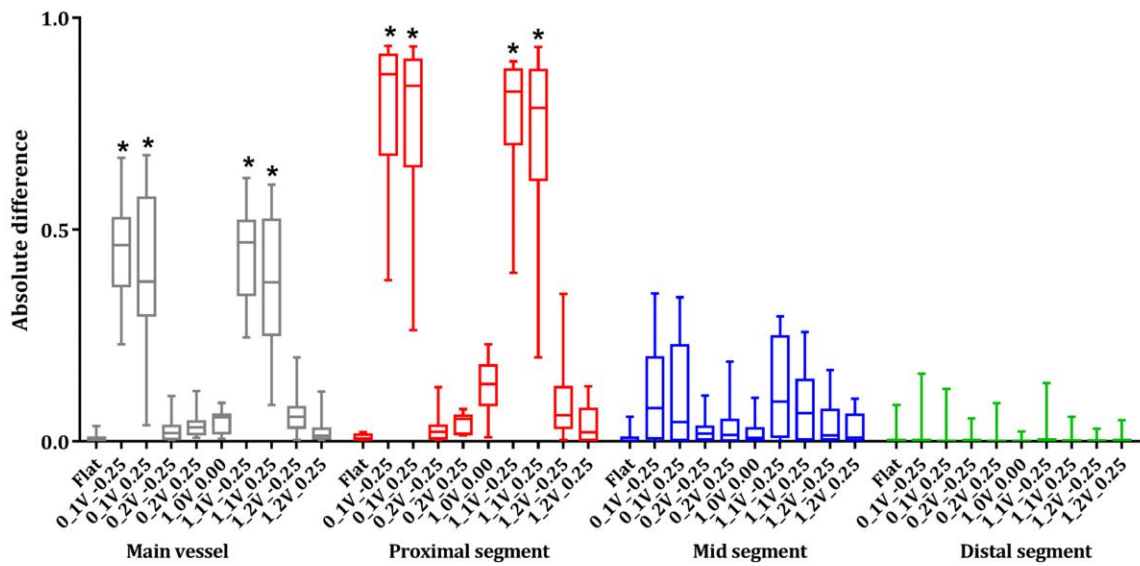
Figure 6. Upper panel: average helicity intensity (h_2) values in the main vessel grouped by geometry and coloured by velocity profile. Lower panel: unsigned balance of counter-rotating structures (h_4) values in the main vessel grouped by geometry and coloured by velocity profile.

Figure 7. Upper panel: from left to right, average helicity intensity (h_2) percentage differences between the reference (0_0V_0.00) and the other velocity profiles in the main vessel, proximal, mid and distal segments. Lower panel: from left to right, unsigned balance of counter-rotating structures (h_4) absolute differences between the reference (0_0V_0.00) and other velocity profiles in the main vessel, proximal, mid and distal segments. Statistically significant differences are indicated with * (p-value<0.001).
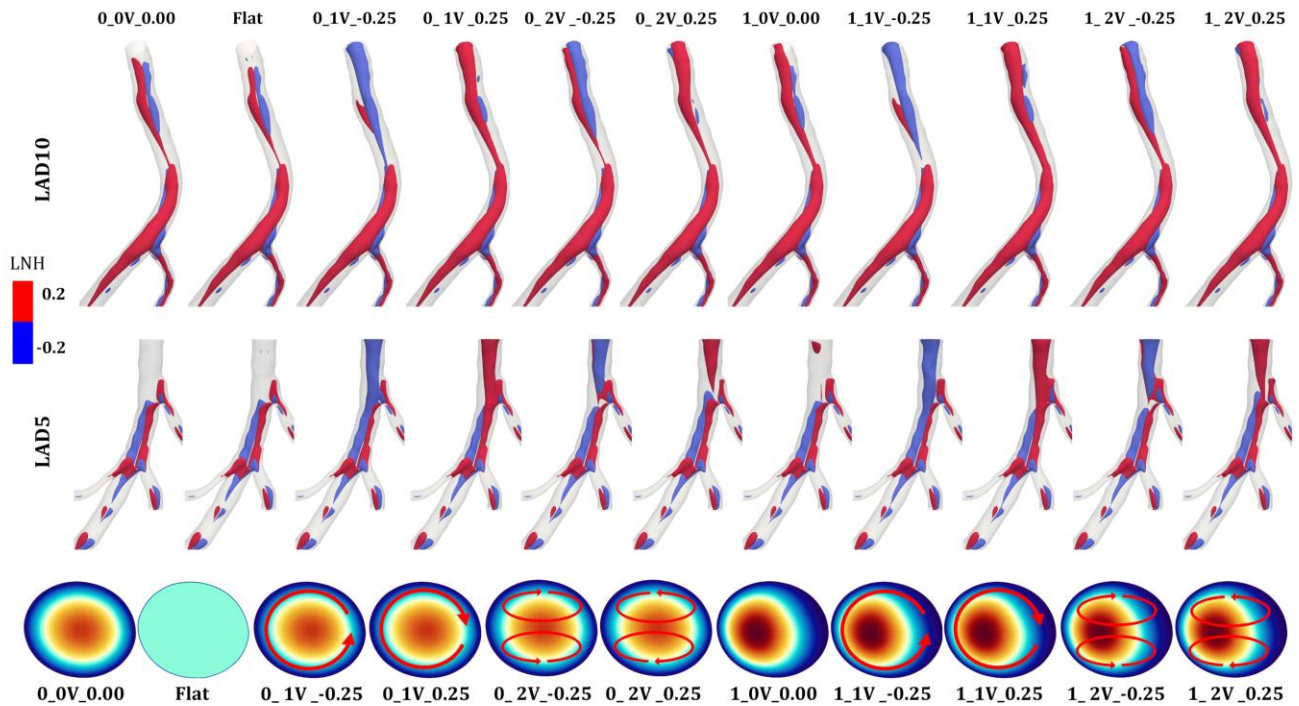
Figure 8. Visualization of intravascular local normalized helicity (LNH) isosurfaces for two explanatory cases (i.e. the models with the lowest and the highest h₂ percentage difference in the main vessel: LAD10 and LAD5, respectively). Right-handed helical structures are associated with positive LNH values (red colour) and left-handed helical structures are associated with negative LNH values (blue colour). A magnified view of the vessels is presented for a clearer visualization of the results.

Tables

Table 1. Impact length *vs* theoretical entrance length

	Impact length (D)	**Theoretical entrance length (D)**
LAD1	5.6	4.4
LAD2	3.2	3.9
LAD3	3.8	5.9
LAD4	3.1	5.0
LAD5	3.0	3.6
LAD6	2.2	3.8
LAD7	2.1	3.7
LAD8	3.1	4.2
LAD9	3.0	3.9
LAD10	3.3	4.1